Advances in Geo-Energy Research

Vol. 20, No. 3, p. 243-258, 2026

Original article

Fluid-pore relationships in tight oil shales: Insights from sequential solvent extraction and advanced rock analysis

Aliya Mukhametdinova[1]*, Bogdan Andreyev[1], Daria Sergeeva[1], Alexander Burukhin[1], Georgy Kalmykov[2], Anton Kalmykov[2], Alexey Cheremisin[1]

[1]*Center for Petroleum Science and Engineering, Skolkovo Institute of Science and Technology, Moscow 121205, Russia*

[2]*Faculty of Geology, Lomonosov Moscow State University, Moscow 119991, Russia*

Keywords:
Oil shale
solvent extraction
nuclear magnetic resonance
rock-eval pyrolysis
microcomputed tomography

Cited as:
Mukhametdinova, A., Andreyev, B., Sergeeva, D., Burukhin, A., Kalmykov, G., Kalmykov, A., Cheremisin, A. Fluid-pore relationships in tight oil shales: Insights from sequential solvent extraction and advanced rock analysis. Advances in Geo-Energy Research, 2026, 20(3): 243-258.
https://doi.org/10.46690/ager.2026.06.06

Abstract:
This study presents an integrated, multi-scale laboratory workflow designed specifically for organic-rich shales using multistage solvent extraction. Applied to oil shales of the Bazhenov Formation of varying maturity and lithology, the key unconventional play in Western Siberia, it enables the construction of a robust, volumetric fluid saturation model. The workflow combines mineralogical characterization, conventional core testing, low-field nuclear magnetic resonance relaxometry, high-resolution X-ray computed microtomography, Rock-Eval pyrolysis, and sequential saturates, aromatics, resins, and asphaltenes fractionation following a three-stage solvent extraction protocol. The core analysis following three-step extraction provides new insights into the interplay between lithology, pore system architecture, and fluid distribution mechanisms within tight, organically heterogeneous media. Key findings highlight that conventional methods often underestimate producible hydrocarbons trapped in kerogen nanopores and asphaltene aggregates, necessitating revised nuclear magnetic resonance interpretation approaches. Mechanically induced porosity, varying with organic matter maturity, is identified and linked to hydrocarbon release and matrix deformation. Combining nuclear magnetic resonance and gas porosity measurements provides a rapid, accurate porosity estimation method with minimal sample alteration. Finally, a conceptual fluid physical model is proposed to better interpret nuclear magnetic resonance data and pore-scale fluid dynamics in similar oil shales. The refined methodology of express core assessment significantly improves industry conventional practices by enabling a more precise and physically meaningful quantification of *in-situ* fluid saturation, including differentiation between bound heavy hydrocarbons and mobile fractions. Beyond advancing the fundamental understanding of fluid saturation and storage capacity in unconventional systems, this framework supports improved reservoir characterization and modeling efforts.

1. Introduction

Despite advances in subsurface characterization, a robust methodology for assessing hard-to-recover reserves in low-permeability organic-rich formations remains elusive (Guo et al., 2024; Hearon et al., 2025) due to lithological heterogeneity, ultra-low permeability, inconsistent evaluation protocols, complex thermal evolution of organic matter (OM), and reliance on limited laboratory techniques that yield conflicting results and underscore the need for methodological integration and cross-validation (Ma et al., 2020).

Among the principal challenges in the development of shale oil resources are the precise determination of key rock properties: OM content, reservoir quality parameters, and

Yandy Scientific Press

*Corresponding author.
E-mail address: a.mukhametdinova@skoltech.ru (A. Mukhametdinova); bogdan.andreyev@ skoltech.ru (B. Andreyev); d.sergeeva@ skoltech.ru (D. Sergeeva); a.burukhin@skoltech.ru (A. Burukhin); gera64@mail.ru (G. Kalmykov).

Received April 15, 2026; revised May 20, 2026; accepted June 2, 2026; available online June 5, 2026.

mechanical behavior under stress conditions. To date, several methodological frameworks have been proposed for evaluating prospective resources not only within the Bazhenov Formation, target oil shale in this study (Petersilie and Komar, 2016; Kalmykov and Balushkina, 2017), but also for unconventional reservoirs globally (Murray and Kuuskraa, 2019). While many frameworks integrate lithological data, petrophysical measurements, and OM characteristics, a comprehensive understanding of fluid dynamics in organic-rich shales requires additional parameters: macro- and microlithological variability, mineral composition, pore morphology, fluid saturation states, wettability, and diagenetic effects on pore-scale fluid distribution.

Notably, the coexistence of relatively high porosity with ultra-low permeability severely limits fluid mobility, thereby reducing the effectiveness of traditional core analysis methods (Shabani et al., 2020). Moreover, extraction processes often require extended durations and may yield incomplete results unless combined with sequential solvent treatments or advanced extraction techniques (Qin et al., 2015; Yang et al., 2021). Additionally, the presence of brittle minerals and high OM content complicates sample handling and preservation, frequently resulting in mechanical damage or hydrocarbon loss during coring and transport that potentially leads to fluid losses of up to 78%, depending on the thermal maturity of the source rock (Zhang et al., 2024). Furthermore, the multiscale nature of the pore system, from nanoscale organic-hosted pores to microscale intergranular voids, requires the application of advanced imaging and analytical tools, such as nuclear magnetic resonance (NMR) relaxometry and micro-computed tomography (μCT), to accurately characterize pore size distribution (PSD), connectivity, and fluid occupancy (Liu et al., 2021; He et al., 2025).

In this context, the objectives of the present study are twofold: (1) to develop a comprehensive, integrated workflow for characterizing pore structure and fluid saturation in organic-rich shales using multistage solvent extraction; and (2) to construct a robust fluid dynamic model specifically adapted for the Bazhenov Oil Shale Formation as a representative case study.

To achieve these objectives, a comprehensive analysis of core samples obtained from three unconventional oil fields, each representing different stages of OM maturity was conducted. Recent studies have demonstrated the value of sequential solvent extraction for evaluating shale oil characteristics (Bai et al., 2023; Tian et al., 2024; Xu et al., 2024). In the present work, these approaches were extended by applying, for the first time, a three-stage solvent extraction workflow to the oil shales of the Bazhenov Formation. The core collection spans maturities from the early to late oil window, enabling an integrated reconstruction of pore-fluid evolution across natural maturity stages using combined petrophysical, hydrocarbons (HC) compositional, and CT-imaging constraints. Compared with previous solvent extraction and NMR studies, the present study introduces several additional components. First, the workflow integrates μCT, saturates, aromatics, resins, and asphaltenes (SARA) fractionation, NMR, and gas porosimetry into a unified maturity-dependent framework. Second, the inverse reconstruction methodology links compositional extraction data with T_1-T_2 hydrogen populations through a mass-balance concept. Third, the study distinguishes between pre-existing pore space and extraction-induced porosity, which becomes increasingly important in mechanically fragile mature shales.

2. Geological setting

The study focuses on the Bazhenov Formation within the central regions of the West Siberian Petroleum Basin (Fig. 1(a)), one of the most extensive and economically significant unconventional hydrocarbon systems globally. The formation consists predominantly of fine-grained, siliceous, organic-rich sediments deposited during the peak of a marine transgression that occurred during the Tithonian to Early Berriasian epochs (Vyssotski et al., 2006).

Stratigraphically, the Bazhenov Formation is traditionally subdivided into six distinct subunits (Fig. 1(b)), differentiated by variations in OM content, clay mineralogy, silica, and carbonate composition (Panchenko et al., 2016). To capture key geochemical and lithological variability, core samples were selected from Subunits IIIVI; the studied intervals are representative of deep-marine, siliceous, and clay-siliceous shales typical for the Bazhenov Formation with total organic carbon (TOC) values above 5 wt.%. OM maturity varies significantly across the sampled wells: Cores from Well #1 correspond to the onset of the oil window, those from Well #2 represent the peak oil generation stage, and samples from Well #3 reflect late catagenesis, as determined by Rock-Eval pyrolysis and vitrinite reflectance analogues. This spatial distribution enables systematic investigation of how thermal evolution affects pore structure and fluid saturation characteristics. Standard petrophysical analyses over the Bazhenov Formation reveal highly variable reservoir properties across the formation, generally characterized by low to moderate porosity ($\phi = 0.05\%$-12%) and ultra-low permeability ($k = 0.006$-1 mD), with marked vertical and lateral heterogeneity (Khamidulin et al., 2012). Samples from Wells #1 and #2 exhibit reservoir properties typical for oil shales, whereas the diagenetically altered carbonate interval in Well #3 displays anomalously high porosity (up to 20%) and permeability exceeding 10 mD in some cases, attributed to secondary porosity features.

3. Core analysis workflow and methods

The object of this study was core material retrieved from the Bazhenov Formation in the central part of the basin from core samples at depths ranging from 230 to 2,655 m. For laboratory experiments, core segments with a diameter of 100 mm were used. These cores were transported in hermetically sealed aluminum tubes ($D = 100$ mm, $L = 1{,}000$ mm) immediately after retrieval to preserve natural fluid saturation during transportation. The core was delivered to the laboratory within one week of drilling.

To minimize the risk of selecting technogenically disturbed intervals and to ensure representative sampling, a comprehensive macroscale X-ray computed tomography scanning was performed directly on the core sections inside the sealed tubes prior to any mechanical handling or unpacking (Fig. 2). Based

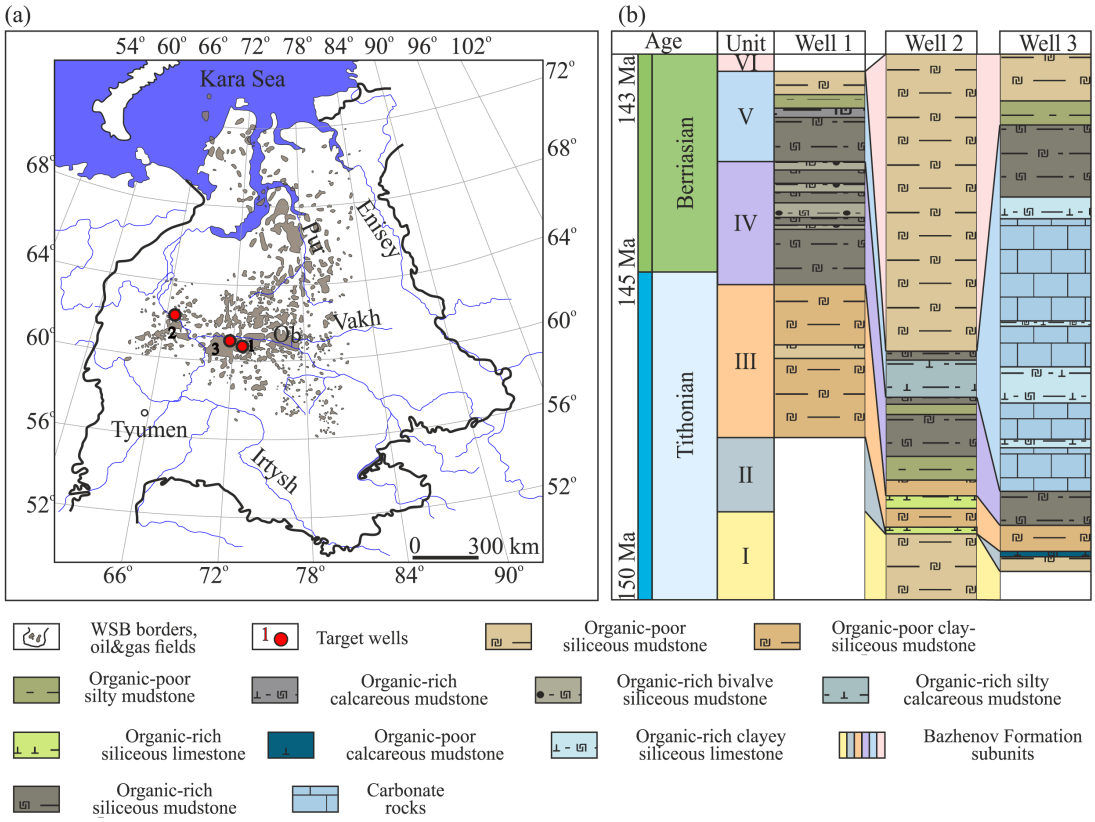

Fig. 1. Map of (a) the West Siberian Basin with the target wells location and (b) lithological sections from the fields.

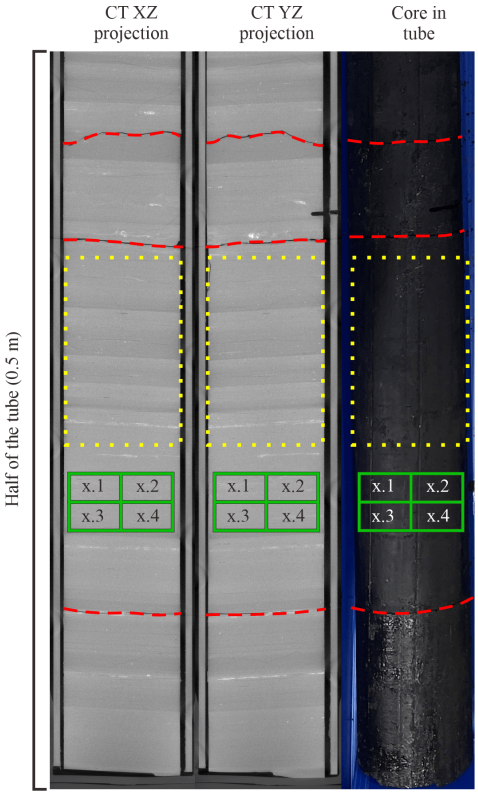

Fig. 2. X-ray tomography of core in the tubes.

on the resulting images, fractured (red lines) or highly heterogeneous intervals (yellow areas) were excluded from further sampling, thereby ensuring maximum preservation of sample integrity throughout the multistage experimental program.

From each selected interval (Fig. 2, two cylindrical samples ($D = 30$ mm, $L = 100$ mm) were drilled at closely adjacent locations and subsequently split into halves for various laboratory analyses (hereafter referred to as petrophysical duplicates). From each original cylinder, two subsamples of standard size ($D = 30$ mm, $L = 30$ mm) were prepared:

1) Two subsamples from cylinder 1 (x.1 and x.2) for conventional core analysis and multistage NMR analysis;
2) Two subsamples from cylinder 2 (x.3 and x.4) for μCT and pyrolysis, thin-section, X-Ray diffraction and fluorescence (XRD and XRF), and other types of analysis.

In total, 13 pairs of cylindrical samples ($D = 30$ mm, $L = 100$ mm) were collected, corresponding to 52 individual specimens of standard size for laboratory testing. The time interval between tube opening, core sampling, and subsequent resealing of the samples ranged from 20 to 30 min. Re-sealing was achieved using multiple layers of paraffin film.

An initial rapid assessment of rock saturation was performed immediately after core samples drilling using low-field NMR relaxometry, combined with Rock-Eval pyrolysis and reservoir properties estimation (Fig. 3). In the second stage, the duplicate samples were allocated for detailed petrographic analyses (including thin section examination, XRF/XRD) and for petrophysical testing such as μCT scanning, gas porosimetry, and further NMR analysis.

This workflow involved multistage solvent extraction

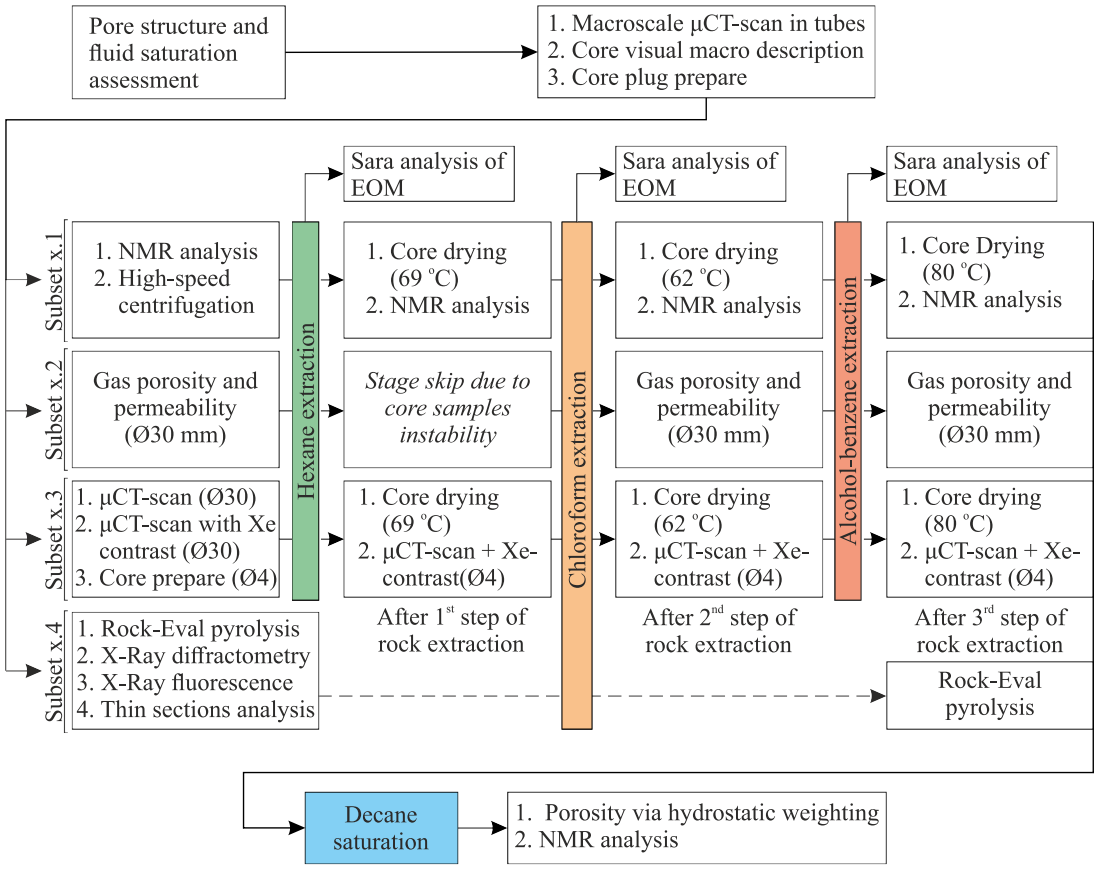

Fig. 3. Experimental workflow of the core analysis.

with solvents of varying polarity (hexane, chloroform, and an alcohol-benzene mixture), followed by sequential NMR, porosimetry, and μCT. The procedure concluded with high-pressure (Decane) saturation to ultimately characterize the rock open and effective porosity.

3.1 Multistage solvent extraction of rock and SARA analysis

A multistage solvent extraction protocol was implemented to systematically isolate various fractions of extractable OM (EOM) from the pore space of the Bazhenov Formation rock samples (Fig. 3). Hot extraction of core samples was conducted using conventional Soxhlet apparatus. The solvent-to-rock ratio during each extraction stage was maintained at approximately 10 : 1 (ml solvent per g rock), which is consistent with standard practices in organic geochemistry core cleaning studies to ensure sufficient solvent accessibility in low-permeability rocks. To maintain extraction efficiency and concentration gradients, the solvent was replaced every 4-5 days during the extraction period. Gravimetric control was performed after each extraction stage using an analytical balance with accuracy of ±0.0001 g. Extraction was considered complete when repeated drying cycles resulted in mass variations below 0.1 wt.%.

The first stage involved extraction of samples with hexane (x.1-x.3) aimed at removing light HC. This process was maintained for 1-3 weeks to ensure thorough extraction until no detectable HC remained. Similarly, the chloroform extraction continued for 4-12 weeks. In the final stage, an alcohol-benzene mixture (1 : 1 vol.) was used to extract additional heavy hydrocarbon fractions, particularly asphaltene and resinous components. This step lasted for 4-8 weeks. Drying temperatures (69, 62, and 80 °C) were selected individually for each solvent system to ensure efficient solvent evaporation at the chemical boiling point of the solvent while minimizing thermal alteration of kerogen and mineral phases. Therefore, the extraction at selected temperatures do not cause significant mineral phase alteration, and kerogen transformation (Zhuoke et al., 2023; Chen et al., 2025). In SARA analysis, after each step of the core extraction the EOM was collected and placed in a rotary evaporator, and the solvent was evaporated under vacuum. To isolate asphaltenes from extracts, the dried chloroform and alcohol-benzene extracts were dissolved in n-hexane (99.5%) for 24 h. After complete dissolution, the mixture was filtered through filter paper, repeatedly rinsing the filter with n-hexane. The fluid passing through the filter paper is considered the maltene fraction. The hexane-insoluble residues remaining on the filter represent the asphaltene fraction. Further separation of maltenes into saturated and aromatic fractions was conducted using glass columns packed with a silica gel (0.04-0.1 mm grain size) and n-hexane (99.5%). Elution was performed sequentially with n-hexane (to obtain the saturated fraction), toluene (to obtain the aromatic fraction), and a toluene-alcohol mixture (1 : 1) to isolate resins.

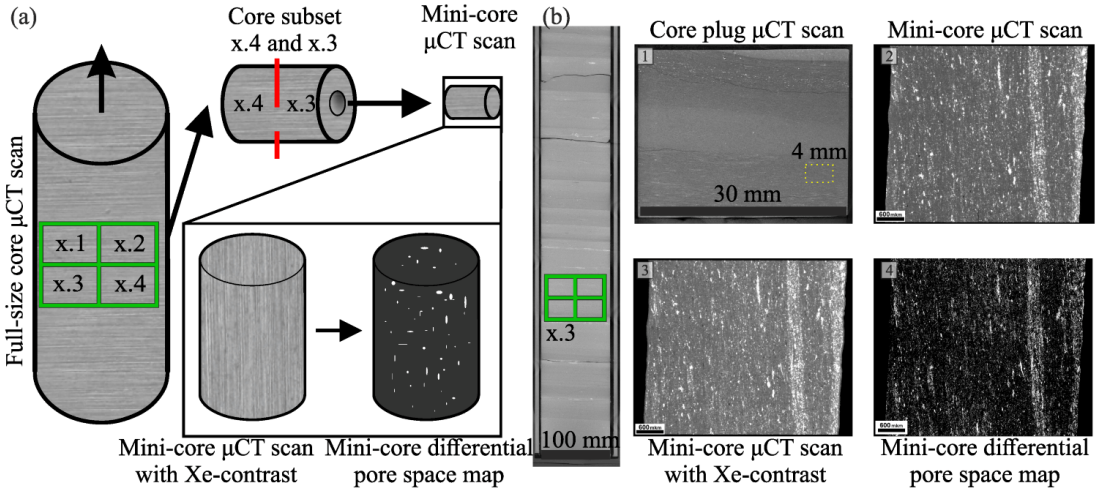

Fig. 4. (a) The workflow of the X-ray computed tomography analysis and (b) obtained scans of the core.

All collected fractions were transferred to separate vials and dried to constant weight with an accuracy of 0.0001 g.

The selection of solvents follows established principles in organic geochemistry, where solubility and polarity govern the partitioning of different hydrocarbon fractions (Tissot and Welte, 1984; Peters et al., 2005). Non-polar hexane preferentially extracts saturated HC, while chloroform, with higher polarity, dissolves aromatic and resinous components. A mixture of alcohol and benzene further targets high-molecular-weight, polar compounds such as asphaltenes, consistent with operational definitions based on solubility behavior (Peters et al., 2005).

3.2 Standard petrophysical measurements

Residual water saturation was determined on core set x.4 using high-speed centrifugation. A Vinci Technologies RC-4500 (France) refrigerated centrifuge was used at 4,500 rpm, with centrifugation times of 24, 48, and 72 h to allow for equilibration of fluid distribution within the pore system. Conventional core studies (gas porosity and permeability measurements) were conducted on core set x.2 using a PIK-PP automated poroperm system (Geologika, Russia), with helium employed as the inert measurement gas. All tests were performed under a confining pressure of 3.4 MPa.

Core saturation with Decane (density: 0.726 g/cm^3 at 24.8 °C) was achieved through a multi-step process that included vacuum degassing, capillary imbibition, and pressure-driven fluid injection. Decane was introduced via capillary imbibition under vacuum, followed by 72 h of pressurized saturation at 15 MPa using an automated saturation system (PIK-SK, Geologika, Russia) with subsequent open porosity measurement.

3.3 NMR relaxometry

A low-field NMR relaxometer, Oxford Instruments Geospec 2/53 (UK), was employed for the analysis of core samples at each stage of the experimental workflow. The system operates at a proton Larmor frequency of 2 MHz, corresponding to a static magnetic field strength of 0.05 T. The method relies on measuring the polarization and subsequent relaxation dynamics of hydrogen atoms present in pore fluids (Callaghan, 1993; Straley et al., 1997). Spin-spin relaxation time (T_2) measurements were obtained using the Carr-Purcell-Meiboom-Gill pulse sequence. The echo spacing (time-echo TE = 2τ) was set to 0.1 ms. For standard T_2 relaxometry, the acquisition parameters included 128 scans (number of scans acquired), a recycle delay of 1,500 ms, and target signal-to-noise ratio of approximately 100. In the case of T_1-T_2 mapping experiments, the number of scans was reduced to between 16 and 32, while the recycle delay was set to 750 ms, resulting in a signal-to-noise ratio of about 50. Raw data were processed and interpreted using Green Imaging Technologies Advanced v.7.5.1 software. The PSD was generated from the T_2 distributions for investigated samples using a surface relaxivity coefficient of 10 µm/s, which remains a widely accepted approximation for shale rocks (Sigal, 2015; Lyu et al., 2018).

3.4 Microscale computed tomography

X-ray computed micro-tomography was carried out on core set x.3 to investigate the changes in the pore space and rock matrix following the core analysis workflow (Fig. 4). Scanning was performed using the GE Phoenix v|tomelx L 240/180 industrial dual-tube X-ray tomography system. The full-sized core, in the sealed aluminum pipes, drilled core plugs and mini-cores were scanned in cone beam mode at the accelerating voltage of 100-180 kV. The geometric resolution was 60 µm per voxel for the full-sized 100 mm diameter core in the steel pipe, 16.5 µm per voxel for the 30 mm diameter core plugs, and 3 µm per voxel for the 4 mm diameter mini-core. The three-dimensional (3D) microtomography images were processed with FEI PerGeos 1.5 software and analyzed by MathMarket GeoDict 2022 software.

To overcome technical limitations, innovative technology of µCT with high-pressure xenon contrasting was applied (Ebadi et al., 2022). The Xenon contrast saturation procedure consisted of two stages: core sample evacuation followed by high-pressure saturation in the coreholder. Samples were first evacuated in a sealed, X-ray transparent cell for 4 h. Xenon

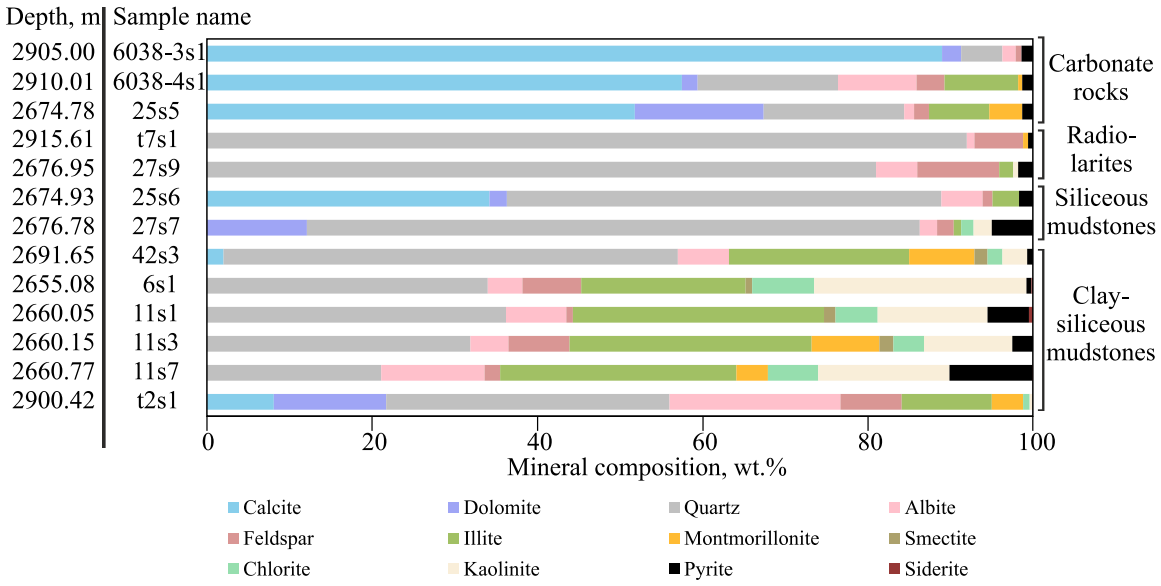

Fig. 5. The results of XRD mineral composition of the rock samples.

was then introduced to a pressure of 2.6 MPa, and samples were saturated for an additional 4 h prior to tomographic imaging.

3.5 Rock-Eval pyrolysis

Rock-Eval pyrolysis (Peters, 1986) was carried out using HAWK pyrolyzer (Wildcat Technologies) operating in bulk-rock mode on the core set x.4. The data interpretation followed standard recommendations on source rock evaluation (Espitalie and Bordenave, 1993). Key output parameters include the amounts of gaseous HC (S_0), light HC (S_1), and heavier hydrocarbon fractions released during kerogen degradation (S_2), all reported in milligrams of HC per gram of rock, the release of carbon monoxide and carbon dioxide during oxidation, recorded as S_3 and S_4, respectively. The temperature at which hydrocarbon generation peaks, known as T_{max}, was determined from the maximum of the S_2 signal. Further analysis provided estimates of TOC, hydrogen index (HI), productivity index, oil saturation index, and the proportion of unconverted kerogen, which together help characterize the source rock potential and OM maturity.

3.6 XRD, XRF, thin sections analysis

Mineralogical composition was determined using XRD analysis of powdered core samples. Measurements were carried out using a benchtop Rigaku MiniFlex 600 X-ray diffractometer (Japan). For more detailed mineralogical characterization of the clay fraction, XRD analysis was conducted on pre-treated samples separated by sedimentation in distilled water (fraction < 0.001 mm). Elemental composition was assessed using sequential vacuum XRF spectrometer Axios^{mAX}-Advanced (PANalytical, Netherlands). XRF results were then recalculated into the oxide form, considering the content of OM in the samples. Optical description and imaging of the thin sections were performed using an Olympus BX53P polarizing microscope (Japan) and an Olympus SZX16 stereomicroscope (Japan).

4. Results

4.1 Rock characterization

4.1.1 Rock lithology and OM characterization

Four distinct lithotypes were identified in the investigated collection of Bazhenov Formation samples through an integrated analysis of thin sections, XRD, and XRF data (Figs. S1 and 5, all results in Tables S1 and S2). The first lithotype consists of carbonate- and OM-rich rocks from the uppermost subunit of the Bazhenov Formation in Well #3 (Fig. S1(b)). Thin section analysis, XRF and XRD data (Table S2) reveal a carbonate rock lacking primary sedimentary structures, likely due to extensive diagenetic overprinting, including recrystallization and pervasive dolomitization. The rock fabric is marked by abundant vugs and microfractures; rare, partially preserved calcareous radiolarian skeletons are observed (Fig. S1(a)), distinguishing this lithotype from the typical Bazhenov Formation facies. The second lithotype is siliceous radiolarite, characterized petrographically by a mottled texture resulting from heterogeneous distribution of OM. Radiolarian skeletons are embedded in a fine-grained matrix composed of siliceous material, which shows partial pyritization (Fig. S1(b)).

The third and fourth lithotypes, distinguished primarily by variable clay content and identifiable only by thin sections, comprise kerogen-rich siliceous and clay-siliceous mudstones. They represent the most widespread and petrographically dominant facies in the Bazhenov Formation. These intervals constitute the main organic-rich zones and are considered key source units. Low detrital admixtures include fine quartz and feldspar grains (up to 5% and more), and OM commonly shows evidence of partial pyritization. This mineralogical signature revealed by XRF and XRD data confirms a more mixed siliceous-clayey composition compared to the radiolarite.

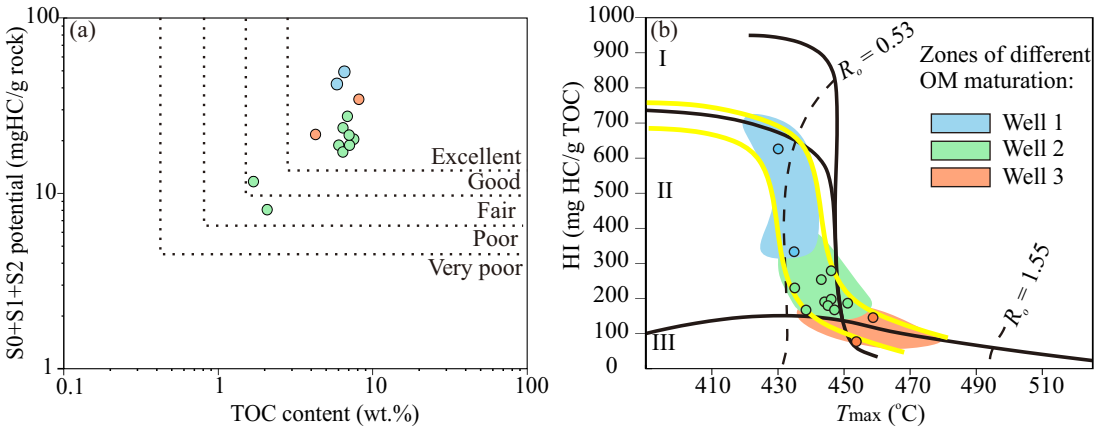

Fig. 6. (a) The source rock generation potential and (b) Van-Krevelen diagram of OM quality; I, II, II-III, III are types of kerogen.

4.1.2 OM: Quality, quantity and maturity

To evaluate the OM characteristics of the Bazhenov Formation across three well locations, Rock-Eval pyrolysis was conducted on the core samples (Table S3). In Well #1 (samples t2s1 and t7s1), TOC values range from 6 to 7 wt.%, which are lower than those observed in immature sections of the Bazhenov Formation (up to 15-20 wt.% according to (Kontorovich et al., 1997; Spasennykh et al., 2021), are accompanied by high HI values of up to 630 mg HC/g TOC. The HI values indicate the hydrogen-rich Type II kerogen derived primarily from marine algal and planktonic OM (Fig. 6). T_{max} values average 430-435 °C, placing the OM within the early oil window.

In Well #2 (samples 6s1, group 11s, group 25s and 27s, 42s3), TOC varies between 1.5 and 7.5 wt.% (average 6 wt.%), with HI values ranging from 200 to 300 mg HC/g TOC. Despite higher thermal maturity, the relatively high TOC and preserved HI indicate deposition in a high-productivity, anoxic environment, with effective OM preservation. T_{max} values range from 438 to 451 °C, indicating progression into the peak oil window. These data suggest that the source rock remains within the main oil window phase, with potential for both oil and early wet gas generation.

In Well #3 (samples 6038-3s1 and 6038-4s1), TOC ranges from 4 to 8 wt.%, but HI values are substantially lower (80-150 mg HC/g TOC). T_{max} values are the highest among the three locations (454-459 °C), reflecting advanced thermal alteration and corresponding to the late oil to early gas window. Although TOC content exceeds the threshold for a viable source rock (> 1.0 wt.%), the reduced HI and elevated maturity indicate that a significant portion of the original kerogen has already undergone conversion and hydrocarbon expulsion.

For the Bazhenov Formation, Rock-Eval T_{max} has proven to be a robust regional maturity indicator when integrated with HI evolution, extract composition. The maturity interpretation used in this study is additionally supported by an extensive regional research results from adjacent wells and basin-scale studies of the Bazhenov Formation (Spasennykh et al., 2021).

4.2 Rock pore structure

4.2.1 Porosity and permeability

Porosity and gas permeability were measured at three critical stages of the core analysis using the pressure pulse decay technique: initially on the as-received (AR) rock samples and subsequently after the second and third (final) solvent extraction and drying. The measurements of porosity and permeability after the first step of extraction (AE-1) were excluded from the testing protocol due to noticeable fragility of the core samples of the x.2 set. The initial porosity values of the rock samples spanned a broad range from 0.6% to 24%, with an average porosity of approximately 3.97% (median = 1.72%, $n = 11$) (Fig. 7, Table S4). Correspondingly, permeability measurements varied between 0.003 and 11.91 mD depending on the lithotype of samples.

Extraction with chloroform (AE-2) resulted in significant increase in open porosity up to 11.4 abs.% (maximum increase for sample 27s7) and 6.7 ± 2.6 abs.% ($n = 11$) in average. However, the gas permeability exhibits noticeable increase for only few samples, probably caused by the formation of cracks; the maximum values were recorded for carbonate sample 6038-3s1 and clay-siliceous mudstone t2s1.

The final post-extraction measurements (AE-3) were performed on about half of the sample collection due to reduced mechanical integrity of the extracted core plugs. The results demonstrated a substantial increase in gas-accessible porosity, on average by 9.2 ± 1.3 abs.% ($n = 6$), indicating that solvent extraction effectively removed previously inaccessible pore space. Permeability values also exhibited a noticeable increase, consistent with enhanced pore connectivity. Sample 27s7 demonstrated a slight decrease in gas porosity after the final extraction stage (AE-3), which is interpreted as a consequence of local compaction of fragile nanopore networks induced by extensive solvent extraction and repeated drying cycles. In contrast, sample 42s3 represents the only case in which permeability decreased after the AE-1 stage despite a continuous increase in porosity. Thin-section observations revealed an initially high abundance of microfractures in this sample, suggesting elevated sensitivity to mechanical disturbance dur-

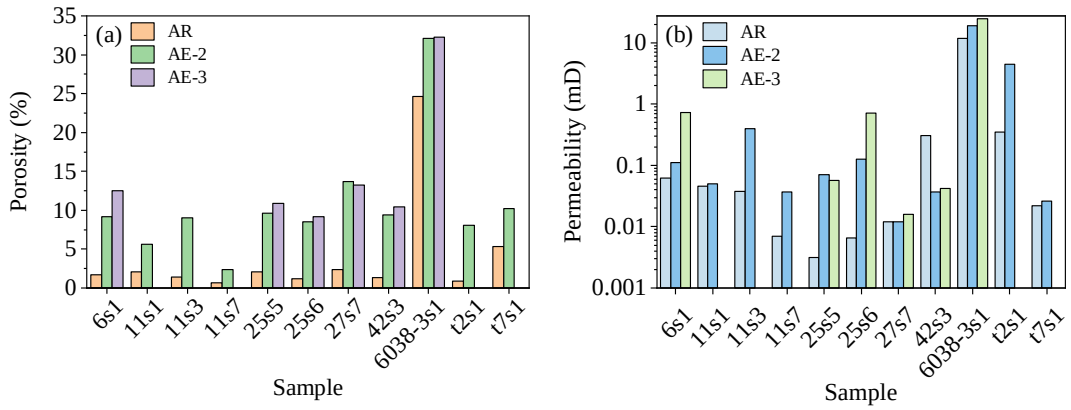

Fig. 7. (a) Rock porosity and (b) permeability (before and after the solvent extraction.

ing extraction and drying. The collapse or disconnection of these fragile conductive pathways likely caused the observed permeability reduction, whereas subsequent hydrocarbon removal continued to increase the total pore volume.

4.2.2 Microscale tomography imaging

Conventional computed microtomography of the Bazhenov Formation rocks on standard core samples provided limited information due to the rock properties, especially when average pore size is below or close to the tomography resolution limits. Therefore, in current research, the advanced technology of contrasting the rock samples with Xe gas was used. Processing the results of the standard and Xe-saturated μCT images by subtracting the original image from the Xe-saturated one provided a map of contrast agent propagation, which could be used as equivalent to an open porosity map (Fig. S2). Due to insufficient resolution obtained on target standard core plugs, the detailed discussion of tomography results was conducted for set of mini-cores with and without Xe contrast.

Differential images for rock samples showed that the initial open porosity can be very limited (e.g., samples 11s3, t2s1) or fragmented and localized (e.g., samples 11s7, 25s5, 25s6) (Fig. S3). In turn, few samples are quite permeable to the contrast agent with a noticeable initial porosity in AR state (e.g., samples 6s1, 42s3, 6038-3s1). After multistage extraction, open porosity increased progressively with solvent polarity (from AE-1 toAE-3), with the maximum rise observed for the least mature sample (t2s1) after the final alcohol-benzene treatment. Large fractures, formed during extraction process, were excluded from analysis (black fractures in Fig. 8).

Excess Xe sorption (up to 150%) in samples like 27s7 reflects kerogen fragments, not open porosity. These micro- and nanoporous kerogen fragments inherently cause excess sorption due to Xe dissolution in residual fluids or adsorption on high-surface-area kerogen (Mayo et al., 2015).

For relatively permeable samples, μCT porosity ($D = 4$ mm) correlates well with gas porosity ($D = 30$ mm) (Table S5). In other samples, gas porosimetry yields significantly lower porosity and permeability for most samples, except the diagenetically altered carbonate. It is explained by the fact that the open pore space is occupied by heavy and liquid HC located in micro- and nanoscale pores, and these HC are removed during the sequential solvent extraction.

μCT analysis confirms that chloroform extraction (AE-2) is necessary to approach true open porosity values (Table S5, Fig. S4). However, absolute porosity values are overestimated compared to other methods, likely due to Xe oversorption in high-TOC samples and analysis of non-identical sample areas. In less mature samples (t2s, 11s7), extraction creates connected porosity by removing heavy HC, but open porosity remains low. In contrast, more mature samples already have an initially connected pore network and yield higher open porosity values.

Despite Xe-assisted μCT's ability to detect pores of any size, porosity and pore size analysis in oil shales remains resolution-limited. In this study, most porosity is associated with pores < 1 μm, yet the μCT scan of 4 mm mini-cores was performed at 3 μm/vox resolution. Therefore, μCT-obtained PSD has limited applicability for the investigated rock collection and for oil shales with similar lithological and geochemical characteristics overall. Furthermore, due to the limited spatial resolution, heterogeneity between analyzed sample volumes, and probable excessive Xe sorption in high-TOC samples resulting in overestimated porosity values, the porosity obtained by μCT was not used in the combined porosity analysis of the target core samples.

However, the PSD registered by μCT at the given resolution can provide insights into pore space evolution in macroscale porosity range within the multistage solvent extraction, as illustrated for the samples t2s1, 11s7, and 27s7 in Fig. S5. The increase in porosity occurs due to either HC extraction and removal, and subsequent enlargement and grouping of small micro-sized pores, which were previously occupied by residual fluid, or mechanical damage of the rock matrix that induces additional artificial porosity.

4.3 Fluid saturation assessment

4.3.1 NMR analysis of fluid saturation

NMR analysis showed that total fluid saturation in AR samples reached up to 2.2 ml, corresponding to a maximum porosity of 11.5% (Fig. 9, Table S6), with an average porosity of $7.7 \pm 2.6\%$ ($n = 13$). The rapid NMR T_2 analysis of AR

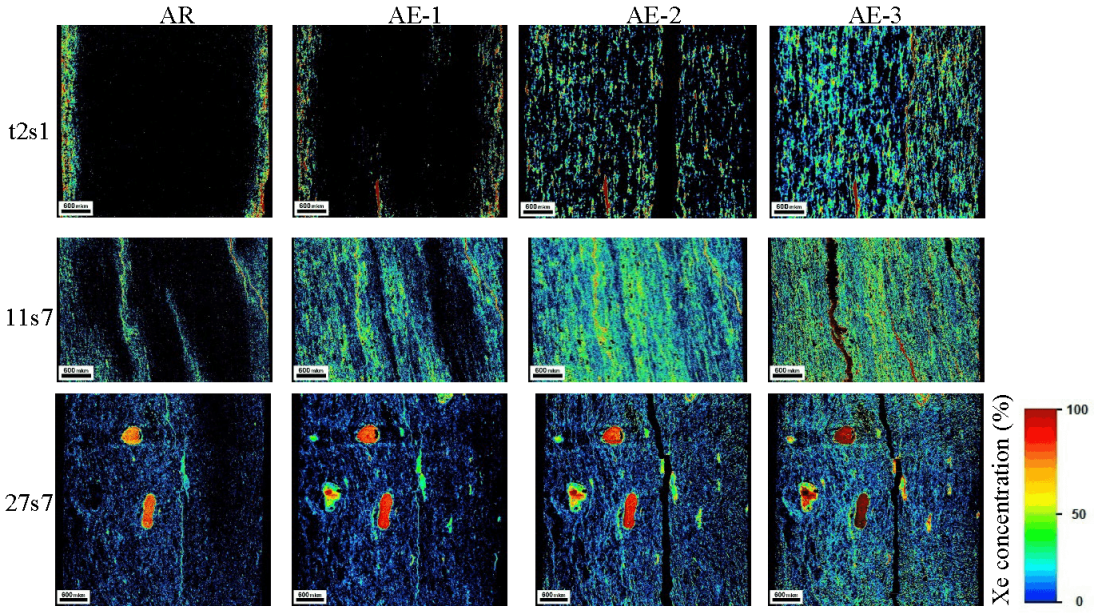

Fig. 8. Differential images for selected samples ($D = 4$ mm). Color scale represents porosity calculated by amount of Xe concentration. The two parts of the sample t2s1 were mechanically sticked together after the second stage of extraction.

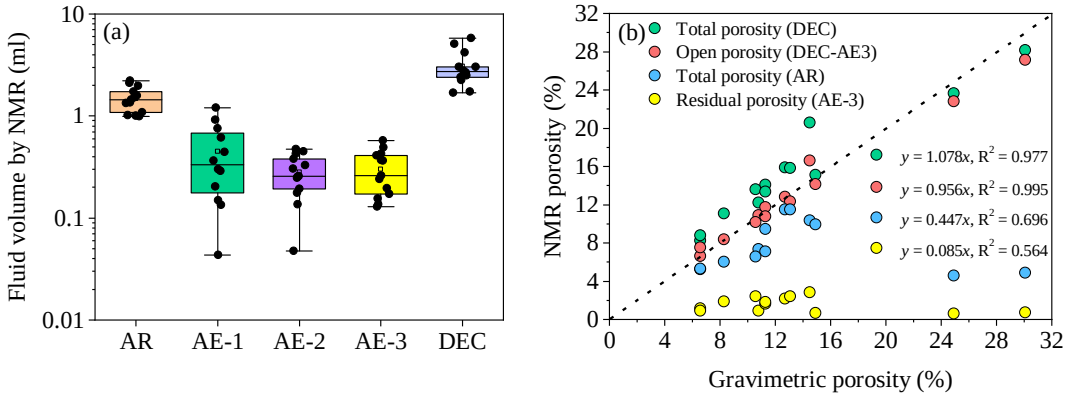

Fig. 9. (a) Fluid saturation and (b) porosity by T_2 NMR for entire collection.

rock enabled registering the volume of residual fluids (HC, water and technical liquids) that mostly occupy pores smaller than 0.1 μm in radius.

Total saturation by NMR registers these fluid types: heavy (asphaltenes and highly viscous components), adsorbed oil, mobile oil (free fluid marked as), clay-bound water, and free water (Li et al., 2020), while the kerogen (and part of solid OM) is not registered by 2 MHz low-field NMR due to its technical limitations and resolution. The highest values of total fluid volume were recorded for the samples 11s1, 11s3 and 42s3 that represent clay-siliceous mudstone. In turn, the carbonates (6038-3s1, 6038-4s1, and 25s5) had the lowest residual saturation and AR porosity by NMR (Table S6) due to preferential loss of light HC during core sampling and storage.

The Fig. 9(a) explicitly demonstrates the gradual change of total fluid saturation in the core samples during the sequential solvent extraction. The slight increase in total fluid saturation after the final extraction stage (AE-3) occurred mainly in samples with high montmorillonite content, likely due to clay swelling and moisture adsorption. This aligns with microtomography results showing geometrical expansion and matrix destruction of 4 mm core plugs.

The total porosity of target collection was defined in AR and Decane-saturated states (DEC), the open porosity is calculated as the signal of Decane-saturated rock after subtracting the dry signal after the final extraction stage (DEC-AE-3). Gravimetric porosity after Decane saturation (Table S7) showed the best consistency with open porosity ($R^2 = 0.995$), confirming the accuracy and precision of the NMR results (Fig. 9(b)).

For detailed analysis of the fluid removal and its redistribution in the pore structure, the T_2-based PSD for selected samples was generated based on the T_2 relaxation curves (Fig. S6) using the fixed surface relaxivity coefficient (ρ) equal to 10 μm/s. Fluid distribution in AR samples depends on OM maturity: in less mature samples, most HC reside in pores of 0.001-0.1 μm (i.e., t2s1 and 11s7), while in more mature samples, fluid occupies pores up to 2 μm (27s7). In general,

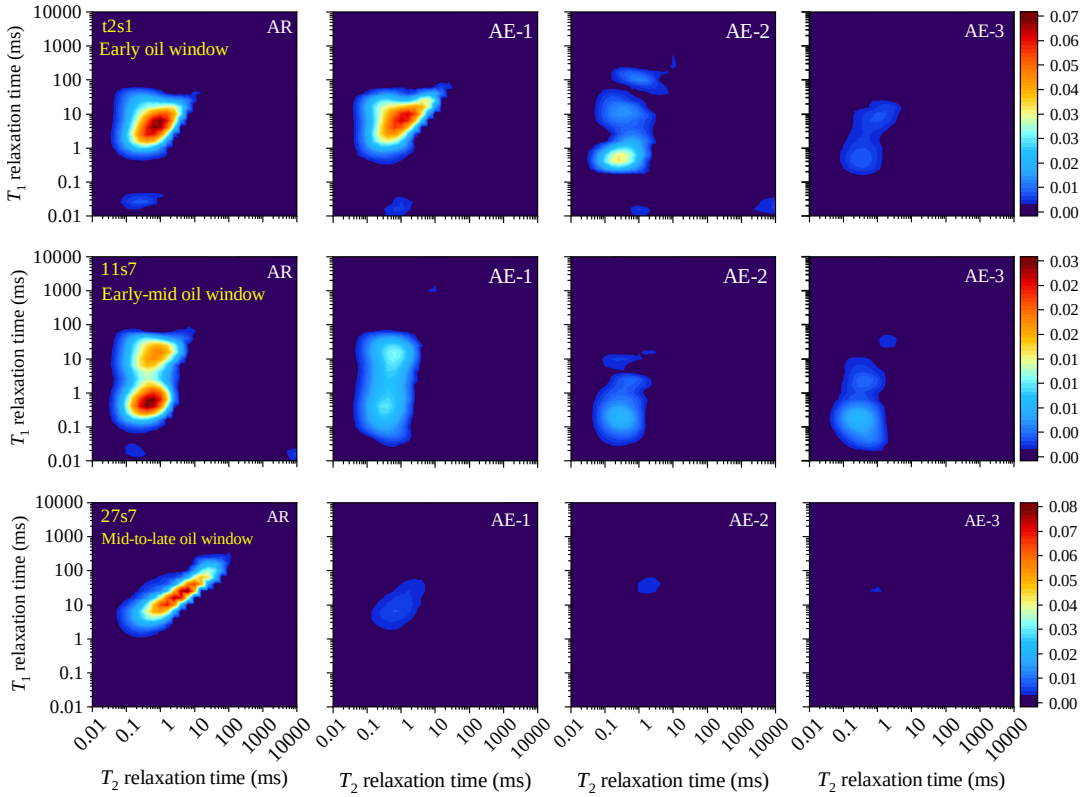

Fig. 10. T_1-T_2 maps for selected samples in different stages of solvent extraction.

the fluid redistribution is observed at all stages of the sequential core cleaning resulting in a relatively smooth decline in total saturation level and removal of fluids from biggest pores after AE-1 to smaller pores after AE-3. After completion of all three steps of extraction, there is a residual fluid explained by remaining heavy HCs and adsorbed moisture: the lowest is registered for the sample with higher OM maturity (27s7). Decane occupies the meso- and macropores up to 25 μm in radius; the obtained PSD is then compared with μCT in the pore range above 2 μm.

The "clay-bound porosity" by T_2 Carr-Purcell-Meiboom-Gill constitutes both heavy & adsorbed OM and clay-bound water which complicates the quantitative analysis for clay-rich shale samples. To separate the hydrogen populations and identify the fluid types, two-dimensional NMR T_1-T_2 maps were constructed for samples immediately after unpacking the tubes (Fig. 10, Table S8). The interpretation followed a scheme adapted from similar geological object in studies reported (Li et al., 2018; Mukhametdinova et al., 2021). This approach allowed differentiation among three primary fluid categories in each sample: high-viscous (heavy) and adsorbed HC, clay-bound water, and mobile HC. For quantitative analysis, T_1-T_2 fractions were calculated based on the total fluid saturation determined from NMR T_2 measurements. High clay content samples show the highest clay-bound water content (up to 12%, average 6%-7%), while mobile HC dominate in carbonate and radiolarite samples. OM maturity affects the speed and extent of hydrocarbon removal during sequential extraction, particularly after the first and second stages. T_1-T_2 maps indicate that most HC are removed by the chloroform stage (AE-2), reducing total saturation near zero. The final alcohol-benzene stage (AE-3) causes additional hydrocarbon removal but also partial matrix destruction and clay swelling, leading to a slight signal increase in montmorillonite-rich samples.

The stage of high-pressure saturation of rock samples with Decane enables tracing the location of mobile HC in the range pore size in Figs. S6 and S7. For samples with pronounced clay-bound fluid regions (e.g., sample 11s7), the map also shows Decane filling the clay interlayers after their partial mechanical disintegration. The comparison of AR and DEC maps in Fig. S7 suggests the development of pore network not only by means of HCs cleaning but also by expansion of porosity caused by the technogenic reasons.

4.3.2 EOM composition

Hexane is a non-polar solvent that dissolved only light (mobile) HC, without affecting polar asphaltene compounds that can block the pore space. The second solvent, chloroform, extracted most of the EOM from open pores. The final extraction in current work utilized the alcohol-benzene mixture that removed the remaining HC. Table S9 and Fig. S8 illustrate that most HC in the rock were removed during AE-1 step using hexane for mature samples. The chloroform proved its efficiency in subsequent core cleaning, especially for low mature clay-siliceous and siliceous mudstone samples with high TOC and clay content.

Dividing the extract into SARA groups provided additional

Table 1. Results of SARA separation of extracts during the multistage core extraction.

No.	AE-1 (hexane) (wt%)				AE-2 (chloroform) (wt%)				AE-3 (alcohol-benzene) (wt%)			
	Saturates	Aromatics	Resins	Asphaltenes	Saturates	Aromatics	Resins	Asphaltenes	Saturates	Aromatics	Resins	Asphaltenes
6038-3s1	83	13	4	0	2	18	24	56	2	1	6	90
6038-4s1	81	14	5	0	12	15	21	53	3	1	4	92
25s5	81	15	4	0	40	33	16	12	1	1	1	98
27s9	85	13	1	0	40	31	19	11	12	10	19	58
25s6	86	12	2	0	53	30	12	5	3	5	3	89
27s7	84	13	2	0	49	30	15	7	8	7	4	81
6s1	85	13	2	0	27	10	49	15	6	3	17	75
11s1	90	9	1	0	69	18	10	3	18	11	13	58
11s3	84	12	4	0	48	24	20	8	10	8	16	66
11s7	77	9	15	0	64	27	7	2	10	12	5	74
t2s1	61	29	10	0	17	38	31	14	4	1	4	91

information on EOM composition and overall efficiency and dynamics of the solvent extraction. For the AE-1 step, three categories (saturates, aromatics and resins) were identified and quantitatively estimated (Table 1). Saturated compounds dominated (61%-90%) in the extract composition, aromatics ranged from 5-29%, and resins - from 1% to 24%. The AE-2 step using chloroform yielded 0.08 to 15.91 mg HC/g, with highest values for sample t2s1. In turn, samples with high EOM mass after AE-1 had lower chloroform yields (1.67 mg/g in 6038-4s1, 1.24 mg/g in 6038-3s1). Maltene fraction dominated in the chloroform extract (85%-98%) for the most samples, except for 6038-4s1 and 6038-3s1, which showed significant asphaltenes (36%-56%). Saturated HC formed most maltenes separated in the EOM for other core samples. The final AE-3 step with alcohol-benzene mixture removed the rest of the fluid, and asphaltenes dominated in this fraction (58%-98%).

5. Discussion

5.1 Fluid saturation dynamics

Low-field NMR, sequential solvent extraction, SARA fractionation, and μCT provide high-resolution characterization of hydrocarbon removal dynamics across a broad maturity range, from early oil to late oil window. Consistent with previous studies on the Bazhenov Formation Formation (Mukhametdinova et al., 2021, 2025), Rock-Eval parameters S_0 and S_0+S_1 correlate with the NMR mobile fluid area, while $S_1+\Delta S_2$ correlates with heavier adsorbed fractions.

The evolution of mobile versus heavy/adsorbed hydrocarbon fractions during sequential extraction (Fig. 11, left) reveals a systematic shift in fluid release mechanisms with increasing thermal maturity. In low-maturity samples, hydrocarbon extraction occurs progressively, with the most significant removal only after chloroform treatment (AE-2). This release pattern, as identified from corresponding 'heavy hydrocarbon area' in T_1-T_2 maps, is classically interpreted as the dominance of polar, high-molecular weight components (resins and asphaltenes) which are adsorbed on the mineral surface and kerogen. In higher-maturity samples, by contrast, rapid and substantial hydrocarbon loss occurs immediately after hexane extraction (AE-1).

This maturity-dependent behavior is further confirmed by SARA compositional trends (Figs. 11(d)-11(f)). In least mature samples, aromatics, resins and asphaltenes constitute most of the total EOM, consistent with incomplete thermal conversion and limited expulsion efficiency. In the case of low maturity, the good correlation was observed between identified areas of "mobile fluid" and "heavy and adsorbed" by NMR with the total EOM. Contrariwise, saturates in more mature samples dominate in the EOM, despite nearly equal total volume of 'mobile fluid' and "heavy and adsorbed" areas.

These findings highlight that hydrocarbon mobility in oil shales is not solely dictated by bulk composition but is critically modulated by nano- and microscale porosity, surface chemistry, OM distribution and maturity. Even relatively short-chain HC can exhibit immobile behavior as identified by NMR, which can be explained by several reasons. First, some potentially mobile light HCs may be trapped within kerogen nanopores or asphaltene aggregates, causing it to appear as high-viscous and adsorbed hydrogen populations in used NMR $T_2/(T_1-T_2)$ interpretation pattern. Thus, relying solely on conventional approaches (such as T_2 cut-offs or T_1-T_2 interpretation schemes in NMR logging) for shale reserves assessment can lead to (1) misinterpretation of recoverable fluids (in terms of group composition and physical properties and (2) underestimation of the potentially producible oil shale reserves.

To visualize this dynamic fluid redistribution, a conceptual model reconstructing initial fluid saturation from the final extraction stage back to the AR state using an inverse stepwise mass balance approach was constructed (Fig. 12). At the final

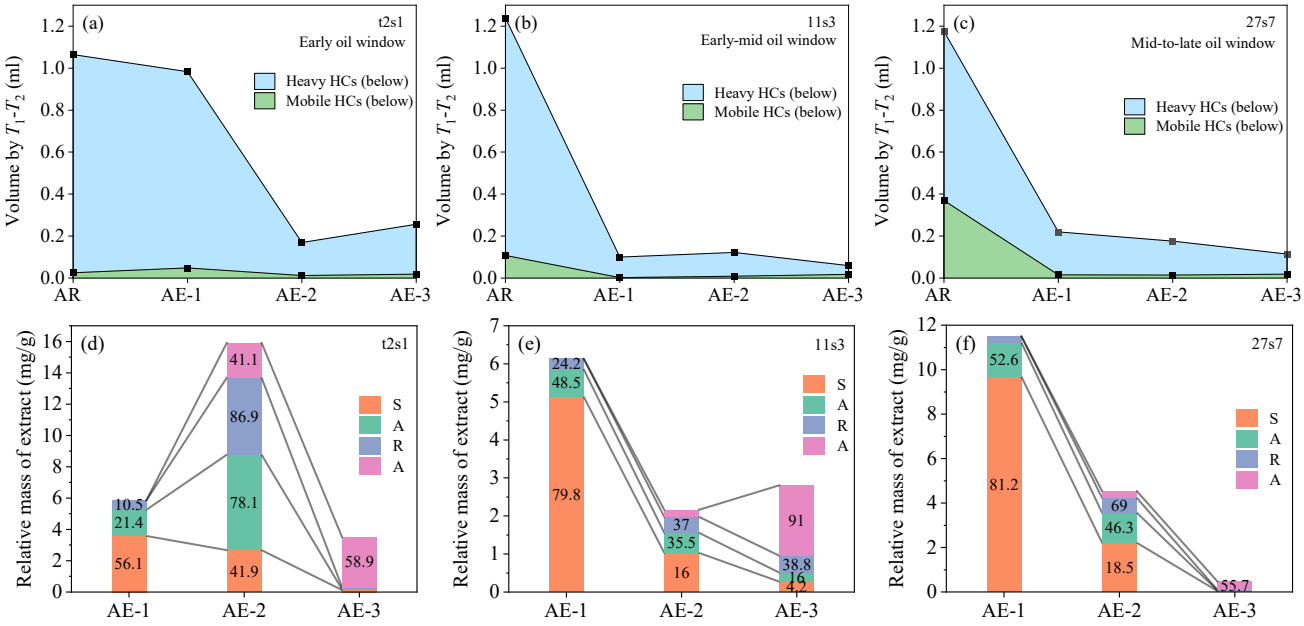

Fig. 11. Composition of the fluid saturation during the sequential core extraction: (a)-(c) By results of NMR analysis for samples t2s1, 11s3, 27s7 and (d)-(f) by results of SARA analysis for samples t2s1, 11s3, 27s7.

extraction stage (AE-3), residual EOM consists predominantly of asphaltenes and resins, which are assigned to the heavy component region in the T_1-T_2 domain. Proceeding backward to the second extraction stage (AE-2), the increase in EOM mass is incorporated by expanding the respective hydrogen populations: Saturates and aromatics populate the mobile fluid zone, while newly extracted components are distributed between heavy and adsorbed regions according to their masses and chemical nature. Finally, the AR state is restored by incorporating the EOM obtained during hexane extraction (AE-1), with saturates and aromatics preferentially assigned to the mobile fluid area and the remainder allocated to adsorbed and trapped domains. This inversion-based methodology, constrained by both compositional (SARA) and petrophysical (NMR) data, provides a qualitative tool for interpreting T_1-T_2 maps in analogous oil shales, bridging molecular-scale oil parameters with pore-scale fluid dynamics.

Despite the integrated nature of the proposed workflow the proposed model can be used only in semi-quantitative way, while several fundamental limitations exist mainly due to the nature of the oil shale systems itself. First, the dominant pore system in the oil shales occurs at the nano-scale, whereas μCT imaging resolution remains limited to the micron scale even with Xe contrasting; therefore, a significant portion of kerogen-hosted nanopores and confined HC cannot be directly visualized. Second, low-field NMR interpretation in organic-rich shales is inherently non-unique because relaxation domains of clay-bound water, adsorbed HC, viscous HC, and kerogen-associated hydrogen populations partially overlap in T_1-T_2 space. Third, sequential solvent extraction and repeated drying may induce technogenic alterations of the rock matrix, including kerogen shrinkage, clay swelling or collapse, pore enlargement, and formation of artificial microfractures.

In practical terms, hydrocarbon removal intensity varies systematically with OM maturity. For mature shale formations, a single extraction step using hexane or chloroform recovers over 70% and over 90% of relevant data, respectively, sufficient for accurate characterization of fluid-rock interactions and pore space estimation. In contrast, less mature shale formations require the full sequential extraction protocol to avoid significant uncertainties in fluid typing and potential inaccuracies in recoverable reserve estimates.

The investigated dataset includes a limited number of representative samples for each maturity stage. Although the selected cores capture the principal maturity evolution trends of the Bazhenov Formation, statistical generalization remains limited due to natural heterogeneity and restricted availability of preserved core material suitable for sequential extraction experiments.

5.2 Alteration of pore space structure

Accurate porosity estimation in oil shales requires integrating multiple techniques employed in the current study. However, each method has inherent limitations, and their comparison reveals important insights about maturity-related artifacts.

Comparing NMR and μCT (Fig. 13(a)), both methods converge above ~ 3 μm for low-maturity samples (t2s1, 11s7), though μCT detects additional macropores from microfractures formed during mini-core handling. For mature samples (27s7), μCT identifies a prominent 3-40 μm pore population absent in NMR data. This discrepancy arises because higher maturity samples exhibit increased mechanical fragility due to kerogen depletion since its thermal degradation weakens rock cohesion through structural changes, an important factor to consider in hydraulic fracturing and development strategies (Othman et al., 2022; Wang et al., 2024). Consequently,

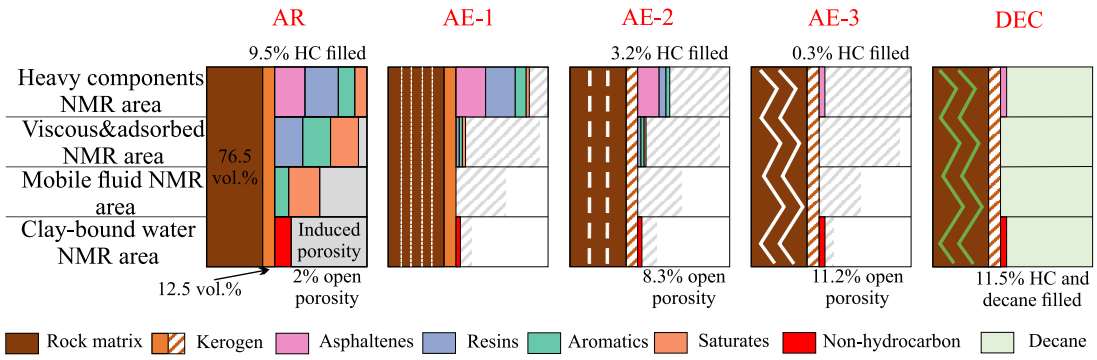

Fig. 12. Fluid composition change over the core extraction protocol and subsequent resaturation on examples of the t2s1 sample (early oil window). The straight and zigzag lines indicate the artificial cracks in the rock matrix; grey dashed area shows the emptied pore space.

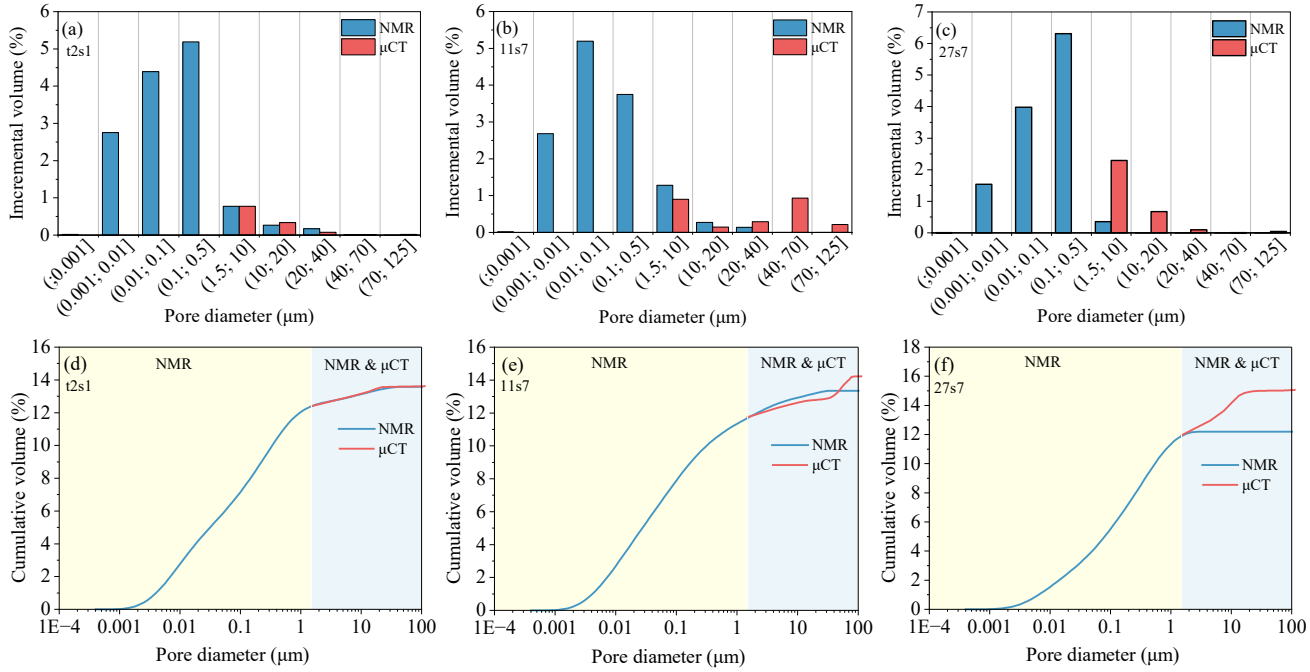

Fig. 13. Differential and cumulative PSDs for selected samples by NMR and μCT: (a) and (d) Sample t2s1, (b) and (e) sample 11s7, (c) and (f) sample 27s7.

μCT measurements on fragile mini-cores risk overestimating porosity through artificial microfractures, whereas NMR on larger, more stable plugs avoids this artifact.

This maturity-dependent fragility also helps explain a seemingly contradictory observation: unlike artificially matured samples (Zhuoke et al., 2023; Liang et al., 2024), naturally matured Bazhenov samples show no significant increase in total porosity with advancing maturity (Table S6), likely due to natural sediment compaction that offsets any secondary porosity generation. Nevertheless, pore connectivity improves markedly, evidenced by a shift toward longer T_2 relaxation times (Fig. S6). Specifically, low-maturity samples are dominated by microporosity (< 10 nm), while higher-maturity samples display enhanced meso- and macropore signals (> 50 nm), indicating coalesced voids and improved percolation pathways. Importantly, effective porosity does not correlate with quartz abundance (Fig. S9), suggesting that soft components (swelling clays, OM) govern porosity more than rigid mineral frameworks. While the direct contribution of OM to porosity remains challenging to isolate due to mechanical disturbance of core samples during the experiment, its role as a structural and chemical mediator cannot be overstated.

Given these complexities, no single method captures the full pore architecture. NMR provides broad sensitivity across the pore size spectrum but cannot distinguish between fluid types without additional steps. Gas porosimetry measures connected pore volume but is unreliable in shales below 1 mD due to extraction- and pressurization-induced damage. μCT offers 3D visualization, yet its ~ 3 μm/voxel resolution even with Xe contrasting misses sub-micron porosity (dominant in oil shales), and as shown above, mini-core preparation risks artificial fracturing in mature samples. Crucially, heterogeneity

in oil shales persists even among petrophysical duplicates, with variations in consolidation state and microfracture density influencing outcomes across different core diameters (4, 30, 100 mm).

To overcome these limitations while preserving sample integrity, a dual-measurement protocol is proposed: combining gas porosimetry and NMR on AR, sealed core plugs immediately after unpacking if possible. The sum of NMR porosity (hydrocarbon-filled voids) and gas porosity (empty pores) estimates total porosity close to post-extraction values (Fig. S10), thus minimizing solvent-induced alterations. This rapid approach is particularly valuable for mature samples as it provides a baseline reference for porosity assessment without excessive core damaging.

Finally, even with optimal protocols, some porosity is only revealed after extraction. Measurable porosity increases by up to 3 abs.% in clay-rich samples following sequential extraction and saturation. The difference in porosity not accounted for by combination of NMR and gas porosimetry values on AR samples is classified as "induced porosity". This "induced porosity" may arise from: (1) New pore formation from removal of asphaltenes and adsorbed components from the kerogen surface; (2) pore enlargement from mechanical effects, crack formation and matrix deformation. Given the capacity to measure total and effective porosity in oil shales, as demonstrated in this study, no existing method currently captures the full PSD in undisturbed oil shale core samples. Even under optimal conditions of preservation, larger pores may lose volatile components during core recovery, biasing initial assessments. In practice, complete separation of these two types of porosity is not possible, as extraction simultaneously removes fluids and mechanically alters the rock fabric. Naturally connected pore systems can be revealed after hydrocarbon removal and detected by NMR, whereas technogenically induced porosity can be captured by μCT and gas porosimetry.

Importantly, petrophysical properties measured after advanced extraction stages do not necessarily represent native reservoir conditions. Consequently, late-stage permeability and porosity values should be interpreted as indicators of accessible or potentially producible pore space rather than initial *in-situ* reservoir properties.

6. Conclusions

This study applied sequential solvent extraction and extended core analysis to Bazhenov Formation oil shales of varying maturity and lithology. By preserving the initial core state, understanding of EOM partitioning and its implications for porosity, fluid mobility, and reservoir evaluation is refined. The major findings include:

1) Conventional NMR-based assessments systematically underestimate producible hydrocarbon volumes in low-maturity samples because mobile phases trapped within kerogen-hosted nanopores and asphaltene-stabilized domains are misclassified as "heavy and adsorbed oil". The identified fluid fractions may contribute to potentially producible HC under appropriate stimulation conditions, thereby necessitating revisions to current NMR $T_2/(T_1\text{-}T_2)$ interpretation models for unconventional systems.
2) Solvent extraction efficiency strongly depends on thermal maturity. In mature samples, single-stage hexane or chloroform extraction recovers $> 70\%$ and $> 90\%$ of EOM, respectively. In lower-maturity samples, extraction occurs progressively, with peak yield only during the second chloroform stage, highlighting the role of polar interactions and molecular confinement in retarding fluid mobilization.
3) μCT resolution limits sensitivity to nanopore-scale fluids and fails to resolve sub-micron pores dominant in low-maturity kerogen, restricting its application in oil shales even with Xe contrasting. In turn, low-field NMR provides broad sensitivity across the pore size spectrum. Consistency between methods in low-maturity samples supports their complementary use; discrepancies in mature samples arise from μCT detecting artificial microfractures formed during core treatment.
4) A hybrid approach combining gas porosimetry and NMR on AR samples provides a rapid, minimally invasive method capturing most accessible pore space while preserving native fluid saturation. However, in low-maturity rocks, a significant portion of porosity remains occluded within unextracted kerogen and is not detectable by low-field NMR, emphasizing the need for post-extraction validation.
5) A conceptual model illustrating fluid model reconstruction and redistribution in oil shales throughout core analysis on the Bazhenov Formation samples is proposed. This framework links molecular-scale properties with observable pore-scale dynamics (by NMR $T_1\text{-}T_2$ mapping), enabling more accurate classification of fluid types based on lithology, maturity, and generated oil composition. The model serves as a transferable tool for refining petrophysical interpretations in analogous oil shale systems.

A streamlined workflow using two to three rapid tests (NMR on AR samples, chloroform extraction, and gas porosimetry) captures over 80% of critical information for practical reservoir evaluation, with significant implications for industrial applications where cost, time, and core availability are limited. This work advances experimental characterization of tight oil shales, enhancing confidence in porosity, saturation, and producibility estimates for digital rock physics, reservoir simulation, and field development planning. Future studies involving larger statistically representative datasets across current and other basins are required to validate the proposed maturity-dependent extraction trends.

Acknowledgements

The authors thank their colleagues: Dr. Natalia Bogdanovich and Prof. Mikhail Spasennykh for help with research design, Dr. Margarita Latypova for help with lithology analysis and core handling, Dr. Elena Kozlova for Rock-Eval analysis, Mr. Andrey Morkovkin for conducting and processing microtomography tests, Dr. Olesia Vidishcheva for help with

SARA analysis, and Mr. Anton Ryabukhin for gas porosity measurements. The authors are grateful to the anonymous reviewers and the editor for their valuable comments and suggestions, which improved the manuscript.

Additional information: Author's email

a.kalmykov@oilmsu.ru (A. Kalmykov);
a.cheremisin@skoltech.ru (A. Cheremisin).

Supplementary file

https://doi.org/10.46690/ager.2026.06.06

Conflicts of interest

The authors declare no competing interest.

References

Bai, L., Liu, B., Fu, X., et al. A new method for evaluating the oil mobility based on the relationship between pore structure and state of oil. Geoscience Frontiers, 2023, 14: 101684.

Callaghan, P. T. Principles of Nuclear Magnetic Resonance Microscopy. Clarendon Press, Oxford, UK, 1993.

Chen, Q., Tang, X., Shi, Y., et al. Nanomechanics and pore structure evolution in organic-rich shale reservoirs during high-temperature treatment: A multi-scale analysis of microscopic stability. Advances in Geo-Energy Research, 2025, 17(3): 241-255.

Ebadi, M., Orlov, D., Alekseev, V., et al. Lift the veil of secrecy in sub-resolved pores by Xe-enhanced computed tomography. Fuel, 2022, 328: 125274.

Espitalie, J., Bordenave, M. L. Screening techniques for source rock evaluation, in Applied Petroleum Geochemistry, edited by M. L. Bordenave, Editions Technip, Paris, pp. 217-278, 1993.

Guo, W., Deng, S., Sun, Y. Recent advances on shale oil and gas exploration and development technologies. Advances in Geo-Energy Research, 2024, 11(2): 81-87.

He, X., Luo, Q., Li, X., et al. Microscopic occurrence mechanism of shale oil in saline lacustrine shale: Insights from NMR and micro-CT combined with saturated oil, centrifuged and solvent extraction experiments. Natural Resources Research, 2025, 34: 2089-2116.

Hearon, J. S., Schenk, C. J., Gelman, S. E., et al. Assessment of conventional and continuous oil and gas resources in the mowry composite total petroleum system in the Southwestern Wyoming Province, Wyoming, Colorado, and Utah, 2024. Reston, VA, U.S. Geological Survey, 2025.

Kalmykov, G. A., Balushkina, N. S. Model of oil saturation of the pore space of rocks of the Bazhenov formation of Western Siberia and its use for assessing the resource potential. Moscow, Russia: GEOS, 2017. (in Russian)

Khamidulin, R. A., Kalmykov, G. A., Korost, D. V., et al. Reservoir properties of the Bazhenov formation. Paper SPE 162094 Presented at the SPE Russian Oil and Gas Exploration and Production Technical Conference and Exhibition, Moscow, Russia, 16-18 October, 2012.

Kontorovich, A. E., Moskvin, V. I., Bostrikov, O. I., et al. Main oil source formations of the West Siberian Basin. Petroleum Geoscience, 1997, 3: 343-358.

Li, J., Huang, W., Lu, S., et al. Nuclear magnetic resonance T_1-T_2 map division method for hydrogen-bearing components in continental shale. Energy & Fuels, 2018, 32: 9043-9054.

Li, J., Jiang, C., Wang, M., et al. Adsorbed and free hydrocarbons in unconventional shale reservoir: A new insight from NMR T_1-T_2 maps. Marine and Petroleum Geology, 2020, 116: 104311.

Liang, Z., Jiang, Z., Xue, Z., et al. Experimental investigation of kerogen structure and heterogeneity during pyrolysis. Geoenergy Science and Engineering, 2024, 242: 213222.

Liu, W., Wang, G., Han, D., et al. Accurate characterization of coal pore and fissure structure based on CT 3D reconstruction and NMR. Journal of Natural Gas Science and Engineering, 2021, 96: 104242.

Lyu, C., Ning, Z., Wang, Q., et al. Application of NMR T_2 to pore size distribution and movable fluid distribution in tight sandstones. Energy & Fuels, 2018, 32: 1395-1405.

Ma, B., Hu, Q., Yang, S., et al. Multiple approaches to quantifying the effective porosity of lacustrine shale oil reservoirs in Bohai Bay Basin, East China. Geofluids, 2020, 2020: 8856620.

Mayo, S., Josh, M., Nesterets, Y., et al. Quantitative microporosity characterization using synchrotron micro-CT and xenon K-edge subtraction in sandstones, carbonates, shales and coal. Fuel, 2015, 154: 167-173.

Mukhametdinova, A., Habina-Skrzyniarz, I., Kazak, A., et al. NMR relaxometry interpretation of source rock liquid saturation – A holistic approach. Marine and Petroleum Geology, 2021, 132: 105165.

Mukhametdinova, A., Markovic, S., Maglevannaia, P., et al. Characterizing low-permeable shales using Rock-Eval pyrolysis and nuclear magnetic resonance for reconstruction of fluid saturation model. Scientific Reports, 2025, 15: 34198.

Murray, B., Kuuskraa, V. A. Bakken shale basin study. Morgantown, WV, National Energy Technology Laboratory, U.S. Department of Energy, 2019.

Othman, A., Glatz, G., Aljawad, M. S., et al. Review of kerogen's geomechanical properties: Experiments and molecular simulation. ACS Omega, 2022, 7: 32829-32839.

Panchenko, I. V., Nemova, V. D., Smirnova, M. E., et al. Stratification and detailed correlation of Bazhenov horizon in the central part of the Western Siberia according to lithological and paleontological core analysis and well logging. Russian Oil and Gas Geology, 2016, 6: 22-34.

Peters, K. E. Guidelines for evaluating petroleum source rock using programmed pyrolysis. American Association of Petroleum Geologists Bulletin, 1986, 70: 318-329.

Peters, K. E., Walters, C. C., Moldowan, J. M. The Biomarker

Guide. Cambridge University Press, Cambridge, UK, 2005.

Petersilie, V. I., Komar, N. V. Algorithm for estimating reserves of shale oil deposits by volumetric method. Russian Oil and Gas Geology, 2016, (5): 95-101.

Qin, H., Ma, J., Qing, W., et al. Shale oil recovery from oil shale sludge using solvent extraction and surfactant washing. Oil Shale, 2015, 32(3): 269-287.

Shabani, M., Krooss, B. M., Hallenberger, M., et al. Petrophysical characterization of low-permeable carbonaceous rocks: Comparison of different experimental methods. Marine and Petroleum Geology, 2020, 122: 104658.

Sigal, R. F. Pore-size distributions for organic-shale-reservoir rocks from nuclear-magnetic-resonance spectra combined with adsorption measurements. SPE Journal, 2015, 20(4): 824-830.

Spasennykh, M., Maglevannaia, P., Kozlova, E., et al. Geochemical trends reflecting hydrocarbon generation, migration and accumulation in unconventional reservoirs based on pyrolysis data (on the example of the Bazhenov formation). Geosciences, 2021, 11(8): 307.

Straley, C., Rossini, D., Vinegar, H. J., et al. Core analysis by low-field NMR. Log Analyst, 1997, 38: 84-94.

Tian, H., He, K., Huangfu, Y., et al. Oil content and mobility in a shale reservoir in Songliao Basin, Northeast China: Insights from combined solvent extraction and NMR methods. Fuel, 2024, 357: 129678.

Tissot, B. P., Welte, D. H. Kerogen: Composition and classification, in Petroleum Formation and Occurrence, edited by B. P. Tissot and D. H. Welte, Springer Berlin Heidelberg, Berlin, pp. 131-159, 1984.

Vyssotski, A. V., Vyssotski, V. N., Nezhdanov, A. A. Evolution of the West Siberian Basin. Marine and Petroleum Geology, 2006, 23: 93-126.

Wang, J., Liu, D., Shi, J., et al. Evolution of mechanical properties of organic-rich shale during thermal maturation. Scientific Reports, 2024, 14: 24327.

Xu, C., Xie, R., Guo, J., et al. Wettability and fluid characterization in shale based on T_1/T_2 variations in solvent extraction experiments. Fuel, 2024, 355: 129512.

Yang, S., Qiao, H., Cheng, B., et al. Solvent extraction efficiency of an Eocene-aged organic-rich lacustrine shale. Marine and Petroleum Geology, 2021, 126: 104941.

Zhang, J., Wang, M., Li, J., et al. Research on loss rules of oil and gas in preserved shale cores after open air exposure. Frontiers in Earth Science, 2024, 12: 1375590.

Zhuoke, L., Lin, T., Liu, X., et al. High-temperature-induced pore system evolution of immature shale with different total organic carbon contents. ACS Omega, 2023, 8: 12773-12786.